www.acsnano.org

# Nonvolatile Phase-Only Transmissive Spatial Light Modulator with Electrical Addressability of Individual Pixels

Zhuoran Fang,\*,<sup>#</sup> Rui Chen,\*,<sup>#</sup> Johannes E. Fröch, Quentin A. A. Tanguy, Asir Intisar Khan, Xiangjin Wu, Virat Tara, Arnab Manna, David Sharp, Christopher Munley, Forrest Miller, Yang Zhao, Sarah Geiger, Karl F. Böhringer, Matthew S. Reynolds, Eric Pop, and Arka Majumdar\*



Downloaded via UNIV OF WASHINGTON on April 28, 2024 at 05:47:12 (UTC). See https://pubs.acs.org/sharingguidelines for options on how to legitimately share published articles.

Cite This: https://doi.org/10.1021/acsnano.4c00340



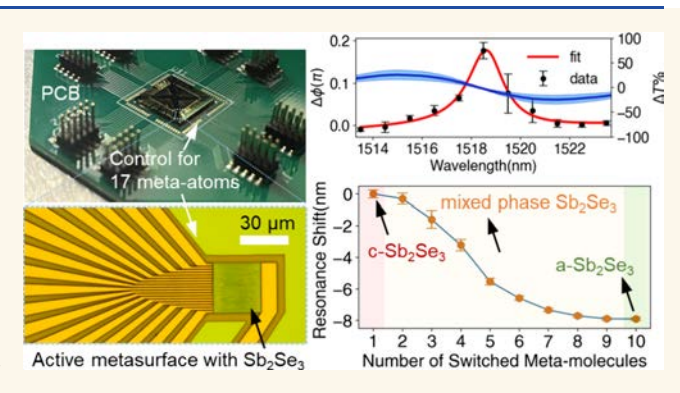
**ACCESS** I

III Metrics & More

Article Recommendations

Supporting Information

ABSTRACT: Active metasurfaces with tunable subwavelength-scale nanoscatterers are promising platforms for high-performance spatial light modulators (SLMs). Among the tuning methods, phase-change materials (PCMs) are attractive because of their nonvolatile, threshold-driven, and drastic optical modulation, rendering zero-static power, crosstalk immunity, and compact pixels. However, current electrically controlled PCM-based metasurfaces are limited to global amplitude modulation, which is insufficient for SLMs. Here, an individual-pixel addressable, transmissive metasurface is experimentally demonstrated using the low-loss PCM Sb<sub>2</sub>Se<sub>3</sub> and doped silicon nanowire heaters. The nanowires simultaneously form a diatomic metasurface, supporting a high-quality-factor



( $\sim$ 406) quasi-bound-state-in-the-continuum mode. A global phase-only modulation of  $\sim$ 0.25 $\pi$  ( $\sim$ 0.2 $\pi$ ) in simulation (experiment) is achieved, showing ten times enhancement. A  $2\pi$  phase shift is further obtained using a guided-mode resonance with enhanced light-Sb<sub>2</sub>Se<sub>3</sub> interaction. Finally, individual-pixel addressability and SLM functionality are demonstrated through deterministic multilevel switching (ten levels) and tunable far-field beam shaping. Our work presents zero-static power transmissive phase-only SLMs, enabled by electrically controlled low-loss PCMs and individual meta-molecule addressable metasurfaces.

KEYWORDS: phase-change materials, nonvolatile, phase-only, transmissive spatial light modulator, electrical individual-pixel control

Free-space modulation of light is a key enabling technology behind optical communications, holography, ranging, and virtual/augmented reality. Traditional spatial light modulators (SLMs) based on liquid crystal (LC) on silicon or microelectro-mechanical systems  $(MEMS)^2$  employ large pixels  $(\sim 10$  $\mu$ m × 10  $\mu$ m), resulting in bulky devices and generally require large driving voltage. To address these limitations, recent years have seen tremendous effort to realize free-space light control based on subwavelength diffractive optical metasurfaces integrated with active materials.<sup>3-12</sup> Metasurfaces can support resonances that enable a substantial phase or amplitude modulation with a small pixel size. Since a smaller active volume is modulated, lower energy and faster modulation speed can be achieved. For example, metasurface resonators ( $Q \sim 550$ ) based on organic electro-optic (EO) polymers have enabled GHz modulation speed, 13 LCs combined with a Huygen's metasurface significantly reduced the pixel size ( $\sim$ 1  $\mu$ m) and LC

thickness ( $\sim$ 1.5  $\mu$ m) required to attain a full  $2\pi$  phase shift range,<sup>3</sup> metasurfaces based on plasmonic resonances coupled to epsilon-near-zero materials have enabled a full  $2\pi$  modulation with independent control of amplitude and phase,<sup>4</sup> and a large phase modulation of  $\sim$ 1.3 $\pi$  was reported by tuning a plasmonic metasurface using graphene.<sup>12</sup> Nevertheless, these approaches are all based on volatile changes, such as the Pockels effect or free carrier dispersion, necessitating a constant power supply to hold the static state. To ensure time-multiplexed pixel control, most of these volatile SLMs require an active memory matrix with

Received: January 9, 2024 Revised: March 27, 2024 Accepted: April 4, 2024



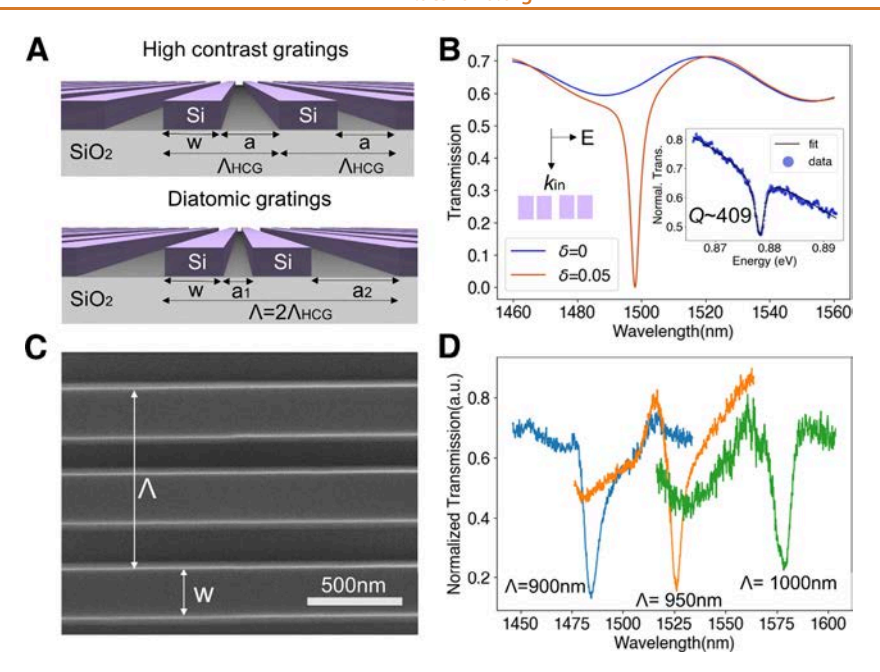


Figure 1. High-Q silicon diatomic metasurfaces. (A) Schematics of the high contrast gratings (top) and diatomic gratings (bottom).  $\Lambda_{\rm HCG}$  and  $\Lambda$  are the periods of the high contrast gratings and diatomic gratings, respectively. The spacing between the gratings is denoted as  $a_1$  and  $a_2$ . w is the grating width. (B) Simulated transmission spectrum of the high contrast gratings (blue) and diatomic gratings (orange) under normal incident TM polarized light. Silicon thickness is 220 nm,  $\Lambda$  = 900 nm, and  $\Gamma$  = 0.7. Inset: experimental spectrum of a resonance fitted by a Fano equation,  $\Lambda$  = 950 nm and  $\Gamma$  = 0.7. (C) Scanning electron microscopy (SEM) of fabricated silicon diatomic gratings. (D) Measured spectra of diatomic gratings with different periods from 900 to 1000 nm, with  $\delta$  = 0.05 and  $\Gamma$  = 0.7.

transistors to hold the written state. In addition, the most prevalent LC-based phase-only SLMs suffer from detrimental pixel crosstalk<sup>14</sup> and temporal phase fluctuations or jitter.<sup>15</sup> To overcome these limitations, a promising solution is to modulate light using nonvolatile materials, which can drastically improve energy efficiency and avoid phase flickering. Moreover, the control complexity can be significantly reduced due to the builtin memory of the nonvolatile reconfiguration. Chalcogenidebased phase-change materials (PCMs) are ideal candidates to realize such functionality, <sup>16</sup> thanks to their nonvolatile microstructural phase transition, <sup>17</sup> large contrast in complex refractive index (typically  $\Delta n \ge 1$ ), <sup>18</sup> and CMOS compatibility. <sup>19</sup> Since PCMs hold their state once configured, a truly "set-and-forget" switching element can be realized. In fact, PCMs have already been used to create tunable metasurfaces for applications such as varifocal lensing, 8,20 beam steering, 21,22 intensity switching, 6,7,23,24 and spectral filtering. 25 Despite the progress, nonvolatile optical phase-only modulation in transmission, a highly desirable feature for SLMs, remains elusive. This is because previous works on nonvolatile tunable metasurfaces have used lossy PCMs such as GST<sup>6,24</sup> or GSST,<sup>7</sup> which concomitantly induce large absorption upon phase transition, prohibiting optical phase-only modulation. The use of metallic heaters further leads to ohmic losses and makes transmissive operation difficult. In fact, to date, all electrically tunable PCM meta-optics have been demonstrated in reflection mode. Although nonvolatile phase-only control has been demonstrated in mid infrared where GST is transparent, 26 the PCM was switched optically, which prevents a fully integrated and scalable platform. A similar work has shown near  $2\pi$  phase shift via optical switching of low-loss PCM Sb<sub>2</sub>S<sub>3</sub> in the visible spectrum,<sup>27</sup> but phase modulation is accompanied by a large amplitude change due to nonnegligible loss of crystalline Sb<sub>2</sub>S<sub>3</sub>.

By leveraging a thin layer (only 20 nm thick) of low-loss PCM Sb<sub>2</sub>Se<sub>3</sub>, we demonstrate a nonvolatile, electrically programmable metasurface for phase-only modulation of free-space near-infrared (NIR) light in transmission. The ultralow loss of Sb<sub>2</sub>Se<sub>3</sub> enables decoupling of the phase modulation from amplitude modulation in NIR. A phase-only modulation of  $\sim 0.25\pi$  in simulation and  $\sim 0.2\pi$  in an experiment is achieved by coupling the PCM to a high-Q diatomic metasurface ( $Q \sim 409$ ). The tunable metasurface also demonstrates large endurance with over ~1000 transitions. We further exploited a guidedmode resonance, albeit with a lower Q-factor, to facilitate a larger electric field overlap with the Sb<sub>2</sub>Se<sub>3</sub> layer, which enabled a full  $2\pi$  phase shift. Beyond global control of the entire metasurface, we show independent electrical control of 17 pixels. A deterministic multilevel resonance tuning of the metasurface is achieved by switching the meta-molecules one by one with a total resonance shift of ~8 nm at a center wavelength of ~1230 nm. By imparting different phase profiles through independently controlling individual pixels, we demonstrate dynamic beam focusing with three distinct focal distances. Our work shows zero-static power transmissive phase-only SLMs using low-loss PCMs and individual-pixel addressable metasurfaces.

## **RESULTS**

**High-Q Silicon Diatomic Metasurfaces.** Sb<sub>2</sub>Se<sub>3</sub> undergoes a refractive index contrast of ~0.7 and exhibits zero loss in both states  $^{28,29}$  near 1550 nm upon phase transition, which stipulates only a ~2.2 μm PCM thickness to obtain a  $2\pi$  phase difference. Although this is significantly thinner than for LCs used in commercial SLMs (>3 μm), it still poses a significant challenge in reversible switching PCMs. As melt-quenching is required to amorphize the material, the integration of thick materials (~50 nm<sup>30</sup>) is precluded, as this limits the required critical cooling rate.<sup>31</sup> Motivated by the use of microring

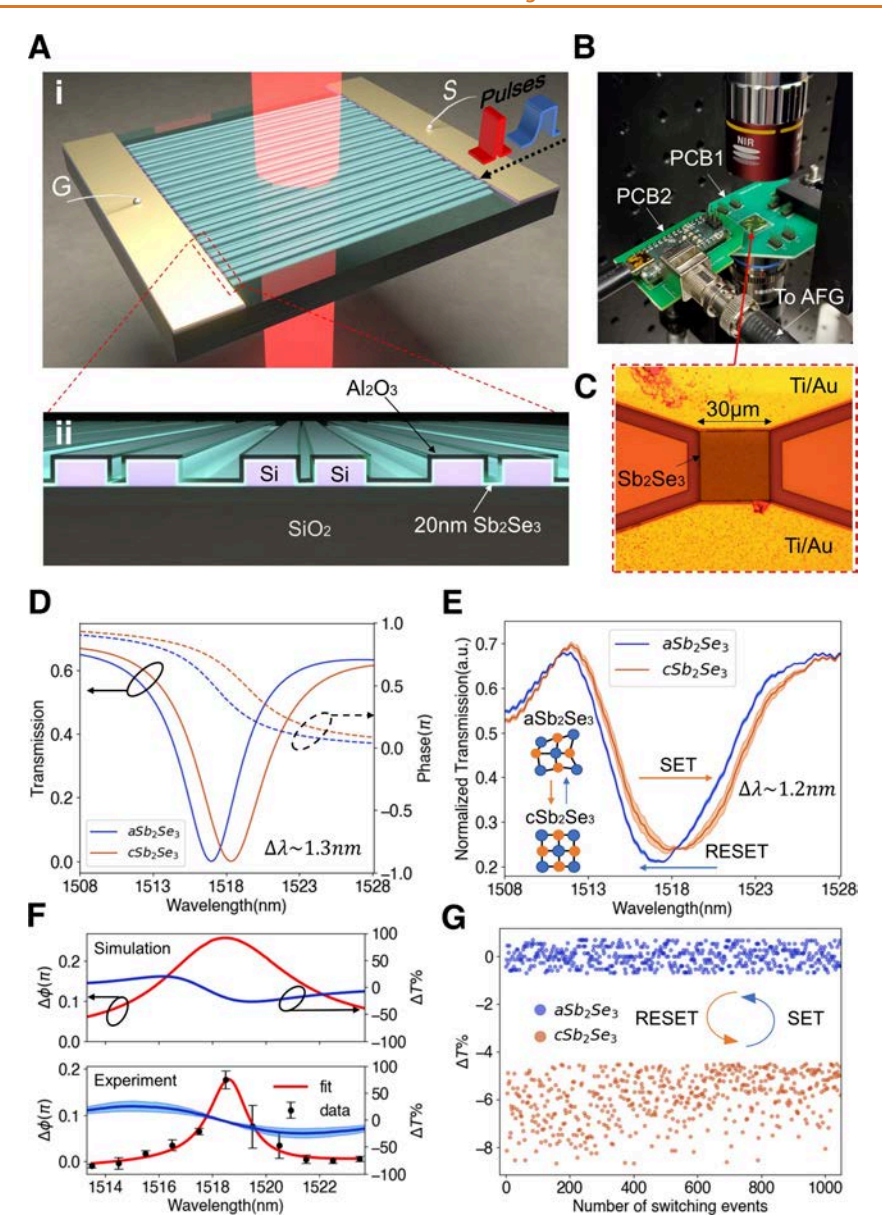


Figure 2. Nonvolatile electrically reconfigurable metasurface based on Sb<sub>2</sub>Se<sub>3</sub>. (A) Schematic of the transmissive tunable diatomic metasurface based on Sb<sub>2</sub>Se<sub>3</sub>. (i) Perspective view. S (G), signal (ground) electrode. (ii) Zoomed-in cross-sectional view. (B) Optical setup for probing the metasurface in transmission along with the devices under the test wire-bonded to a customized PCB. AFG is an arbitrary function generator. (C) Optical micrograph of a single metasurface on the chip under test. (D) Simulated spectral and phase shift caused by the phase transition of 20 nm thick Sb<sub>2</sub>Se<sub>3</sub>.  $\Delta\lambda$  is the wavelength shift of the resonance dip. The diatomic metasurface is designed to have  $\Lambda$  = 900 nm,  $\Gamma$  = 0.7, and  $\delta$  = 0.05. a(c)Sb<sub>2</sub>Se<sub>3</sub>: amorphous(crystalline) Sb<sub>2</sub>Se<sub>3</sub>. (E) Measured reversible switching of the diatomic resonance. The switching conditions are 3.6 V (5.1 mA), 50  $\mu$ s pulse width, 30  $\mu$ s trailing edge with energy of 11.1  $\mu$ J for SET and 11.6 V (16.6 mA), 1  $\mu$ s pulse width, and 8 ns trailing edge with an energy of 1.9  $\mu$ J for RESET. Three consecutive cycles are plotted where the shaded area indicates the standard deviation between the cycles, and the solid line indicates the average. The spectrum is normalized with that of bare SiO<sub>2</sub> on silicon. (F) Phase shift ( $\Delta\phi$ , red) and transmission contrast ( $\Delta$ T%, blue) between two optical states extracted from the simulation (top) and experiment (bottom). The phase is measured at 11 different wavelengths with 1 nm spacing and averaged over three switching cycles. The standard deviation over the cycles is shown by the error bars. (G) Cyclability of the tunable metasurface for 1000 switching events. The switching conditions are the same as those for panel E. Each pulse is temporally separated by 2 s to ensure long thermal relaxation. The data are filtered by a two-point moving average to reduce fluctuation caused by thermal and mechanical noises.

resonators to increase the modulation contrast in integrated photonics, <sup>32</sup> a high-Q meta-optical resonator can be used to enhance the phase modulation of free-space light by thin film PCMs while allowing thinner device layers than traditional Fabry—Perot cavities. Earlier works on high-Q meta-optical resonators focused on high contrast gratings (HCGs), <sup>33</sup> whereas recent works studied quasi-bound-state-in-the-continuum (q-BIC) in periodic nanostructures with in-plane asymmetry. <sup>34,35</sup>

Here, we combine the idea of HCGs and q-BIC by introducing asymmetry into the periodicity of traditional HCGs, realizing a diatomic metasurface (Figure 1A). Although such diatomic metasurfaces have been explored in theory,  $^{36-38}$  thus far, the experimental demonstration of this concept has been missing. Figure 1A shows how the symmetry of the HCG is broken by slightly displacing one of the gratings relative to the other such that the grating spacing becomes dissimilar, i.e.,  $a_1 \neq a_2$ . We

denote the displacement or perturbation by  $\delta = \frac{a_2 - a_1}{\Lambda}$  where  $\Lambda$ is the period of the diatomic grating, with  $\delta$  = 0 denoting a simple HCG. The duty cycle  $\Gamma$  is defined as  $\frac{w}{\Lambda_{HCG}}$  for HCGs and  $\frac{2w}{\Lambda}$  for diatomic gratings, where w is the grating width. We note that  $\Gamma$  is essentially identical for both types of gratings because the period of diatomic gratings is twice that of the HCG. The periodicity doubling causes the folding of the first Brillouin zone such that dark modes that were originally at the edge of the Brillouin zone outside the light cones get folded into the interior of the light cones, allowing for free-space excitation.<sup>36,37</sup> Figure 1B shows the simulated spectral response of HCGs ( $\delta = 0$ ) and diatomic gratings ( $\delta = 0.05$ ) upon excitation of normal incident transverse-magnetic (TM) polarized light near 1550 nm wavelength ( $\Lambda$  = 900 nm and  $\Gamma$  = 0.7). When  $\delta$  = 0, the dark modes are not accessible to the free-space excitation, and hence, no resonance is observed. Meanwhile, a small perturbation of  $\delta$  = 0.05 is enough to introduce a sharp q-BIC resonance<sup>36</sup> with its signature Fano line shape. The pronounced resonance is also clearly visible in Supplementary Figure S1, where the q-BIC resonance represents ~40× electric field enhancement compared to the  $\delta$  = 0 case. By fitting the experimentally measured resonance, we extract a large Q factor of 409 for heavily N-doped 220 nm thick silicon-on-insulator (SOI), as shown by the inset of Figure 1B. We note that the doping is necessary for the electrical actuation of the phase transition in the PCM. <sup>39,40</sup> Such a high experimental Q factor is attributed to the q-BIC mode and ultrasmooth etching side wall as revealed by Figure 1C, despite the additional loss from the doping. Figure 1D shows the experimentally measured resonances as the period increases from 900 to 1000 nm (silicon thickness of 220 nm,  $\delta$  = 0.05 and  $\Gamma$  = 0.7). The resonance almost linearly shifts across the telecommunication wavelength range without a significant change in the Q factor, a highly desirable characteristic of diatomic gratings.<sup>36</sup> In contrast, changing the period of HCGs

The diatomic metasurface makes an ideal platform for demonstrating nonvolatile phase-only modulation with low-loss PCMs for two reasons. First, meta-atoms of equal width w allow identical microheater resistance, which is essential for uniform heating of PCMs cladded on top. In comparison, meta-atoms of dissimilar width or with additional notches<sup>41</sup> can also facilitate high Q resonances, but will ultimately give rise to different resistances in the heater resulting in a nonuniform Joule heating from current injection. Second, the resonance can be fine-tuned to an arbitrary wavelength by changing the period without degrading the Q factor, similar to changing the radius of a microring in integrated photonics, which enables operation over a large wavelength range limited only by the material bandgap.

will lead to a dramatic change in the Q factor as reported

previously.<sup>33</sup>

Nonvolatile Electrically Controlled Global Phase-Only Modulation. To dynamically control the diatomic metasurface, we dope the SOI to create microheaters  $^{39,42}$  (phosphorus doping concentration  $\sim 10^{20}$  cm $^{-3}$ ) that can switch the Sb<sub>2</sub>Se<sub>3</sub> cladded on top (Figure 2A). This doped silicon is then etched into the diatomic metasurface, before depositing 20 nm of Sb<sub>2</sub>Se<sub>3</sub> via sputtering, followed by 40 nm of atomic-layer-deposited (ALD) Al<sub>2</sub>O<sub>3</sub> encapsulation to prevent oxidation and PCM dewetting during switching (see Methods for details on fabrication). Ohmic contacts are then formed by Ti/Au electrodes. The cross-section of the metasurface is shown in Figure 2A(ii). Current is injected into the highly doped silicon

gratings via electrical pulses that causes joule heating, which in turn switches the PCM. The measured resistance of this metasurface is  $\sim 70\Omega$ . A two-objective transmission setup (see Methods for details on the measurement setup) is used to probe the reversible switching of the Sb<sub>2</sub>Se<sub>3</sub>-loaded diatomic metasurface. The fabricated chip is wire-bonded to a customized printed circuit board (PCB) (labeled PCB1 in Figure 2B) connected to a second customized PCB carrying a microcontroller (labeled PCB2 in Figure 2B). PCB2 is then connected to an arbitrary function generator (AFG). The microcontroller on the PCB2 can be programmed to individually address each metasurface pixel, or meta-atoms (see Methods for details on the electrical control). Figure 2C shows the optical micrograph of a 30  $\mu$ m aperture metasurface on a chip that has been wire-bonded to the PCB. Reversible tuning of the diatomic resonance is shown in Figure 2D (simulation) and Figure 2E (experiment). The spectra of three consecutive switching cycles are plotted in Figure 2E and the shaded regions indicate standard deviations between the cycles. The small standard deviation reveals excellent cycle-to-cycle reproducibility. The experimentally extracted spectral shift ( $\Delta \lambda \sim 1.2$  nm) matches very well with the simulated shift ( $\Delta\lambda \sim 1.3$  nm). Figure 2F shows the phase shift  $(\Delta \phi)$  and transmission contrast  $(\Delta T\%)$  between the two optical states near the 1518 nm resonance. A good agreement between the simulation and experiment can be clearly observed. We extract a maximum phase shift of  $\sim 0.2\pi$  ( $\sim 0.25\pi$ ) near the resonance wavelength via the digital holography experiment (simulation) with less than 10% measured change in transmission (see Methods for details on the spectra and phase-shift measurement). We note that this phase shift is  $\sim 10$  times larger than what can be achieved by switching a 20 nm thick blanket film of Sb<sub>2</sub>Se<sub>3</sub> without a metasurface. To further show that this is indeed a phase-only modulation, we fit the Fano line shape to the resonances of aSb<sub>2</sub>Se<sub>3</sub> and cSb<sub>2</sub>Se<sub>3</sub> averaged over five consecutive cycles (Supplementary Figure S2). The extracted Q factor decreases from 312 to 271 upon crystallization, which shows that minimal loss is introduced by the phase transition. In contrast, the resonance is completely suppressed by the same thickness of GST cladded on the metasurface due to high absorption in GST (Supplementary Figure S3). Temporal trace measurements (Supplementary Figure S4) also confirm that the change is indeed nonvolatile and hence caused by the Sb<sub>2</sub>Se<sub>3</sub>. Finally, we show that the tunable metasurface maintains its functionality and is robust for over 1000 switching events, without degradation in contrast, as shown in Figure 2G, where a tunable laser is set to a wavelength near the resonance to detect a measurable change of  $\sim 6\% \pm 1\%$  in transmission (see Methods for details on the cyclability test). Furthermore, optical micrographs taken before and after the cyclability test indicate no ablation occurred by the switching across the entire 30  $\mu$ m  $\times$ 30  $\mu$ m metasurface (Supplementary Figure S5). Apart from switching Sb<sub>2</sub>Se<sub>3</sub>, we also show that the doped silicon microheater is a versatile platform for switching other PCMs, for example, we have also reversibly switched GST using a doped silicon microheaters on a sapphire substrate to realize a broadband tunable notch filter in transmission, see Supplementary Figure S6.

Full  $2\pi$  Phase Shift and Individual-Pixel Control. In the same diatomic grating structure, we observed a transverse-electric (TE) polarized guided-mode resonance at ~1238 nm with enhanced interaction with Sb<sub>2</sub>Se<sub>3</sub>, achieving a larger resonance shift (~10 nm) and a full  $2\pi$  phase shift in simulation (Supplementary Figure S7), albeit at the expense of a lower Q-

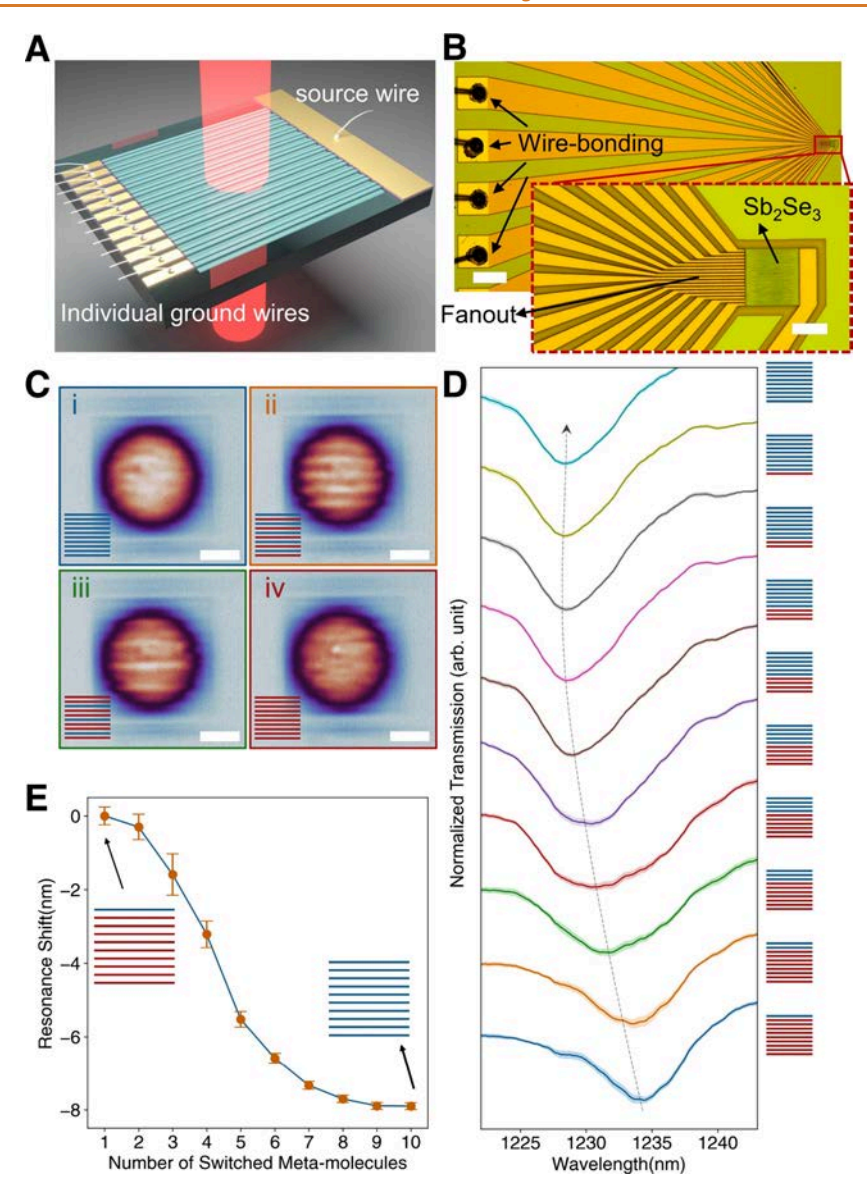


Figure 3. Individual control of pixels or meta-molecules. (A) Schematic of the individually controlled meta-molecules. (B) Optical micrographs of the metasurface with individual meta-molecule controllability (scale bar:  $200\,\mu\text{m}$ ), where each channel is wire-bonded to contact on PCB1. Inset: Zoomed-in optical micrograph (scale bar:  $20\,\mu\text{m}$ ) showing the fanout of 17 electrical channels from the metasurface. (C) IR camera images showing four different metasurface configurations (scale bar:  $10\,\mu\text{m}$ ), indicated by the insets at the bottom left corner of each subplot. The circular shape is due to the finite area illuminated by the focused Gaussian beam. The bright (dark) lines show amorphous (crystalline) Sb<sub>2</sub>Se<sub>3</sub> due to the slight absorption difference. The switching conditions are 6 V ( $\sim$ 4.1 mA per channel), 50  $\mu$ s pulse width, 30  $\mu$ s trailing edge, with 1.5  $\mu$ J energy per channel for SET and 15 V ( $\sim$ 10.3 mA per channel), 1.25  $\mu$ s pulse width, 8 ns trailing edge with 0.2  $\mu$ J energy per channel for RESET. (D) Waterfall plot for the normalized transmission spectra as the meta-molecules are switched individually. The pulse conditions are the same as those in panel C. The result is averaged over nine repeated cycles, and the shaded region indicates the standard deviation. Each spectrum is vertically offset for clarity. (E) Fitted Fano-resonance spectral shift with respect to the number of channels switched. The resonance wavelength gradually blue shifts as more gratings are switched. The small error bar indicates a deterministic multilevel operation. (arb. unit: arbitrary unit).

factor ( $\sim$ 100) than that of the q-BIC mode. We note that this resonance mode requires a slight incident angle ( $\sim$ 3°) to couple the incident light to the metasurface (Supplementary Figure S7). When the incident angle is less than 3 degrees, the resonance is barely visible in the simulation, indicating a dark mode. As the angle increases, the resonance red shifts and gradually broadens (see the energy-momentum spectrum or E-k spectrum in Supplementary Figure S7). The 3-degree incident angle trades off a lower *Q*-factor for a more apparent resonance.

By now, we have established global phase-only modulation in transmission of the entire metasurface, whereas spatial light modulation requires independent control of each pixel. Here, we demonstrate the independent addressing of pixels (or metamolecules), defined as two diatoms with a total pitch of 1.8  $\mu$ m, to control the optical wavefront spatially and spectrally. The individual control is realized using a single source channel and 17 separate ground channels connected to 17 meta-molecules, see Figure 3A,B. The channels fanned out from the metasurface are electrically isolated by overetching the silicon into the buried oxide and are wire-bonded to PCB 1, as shown in Figure 2B. We note that the number of channels used here is arbitrary and is only limited by our PCB design. The source channel delivers the

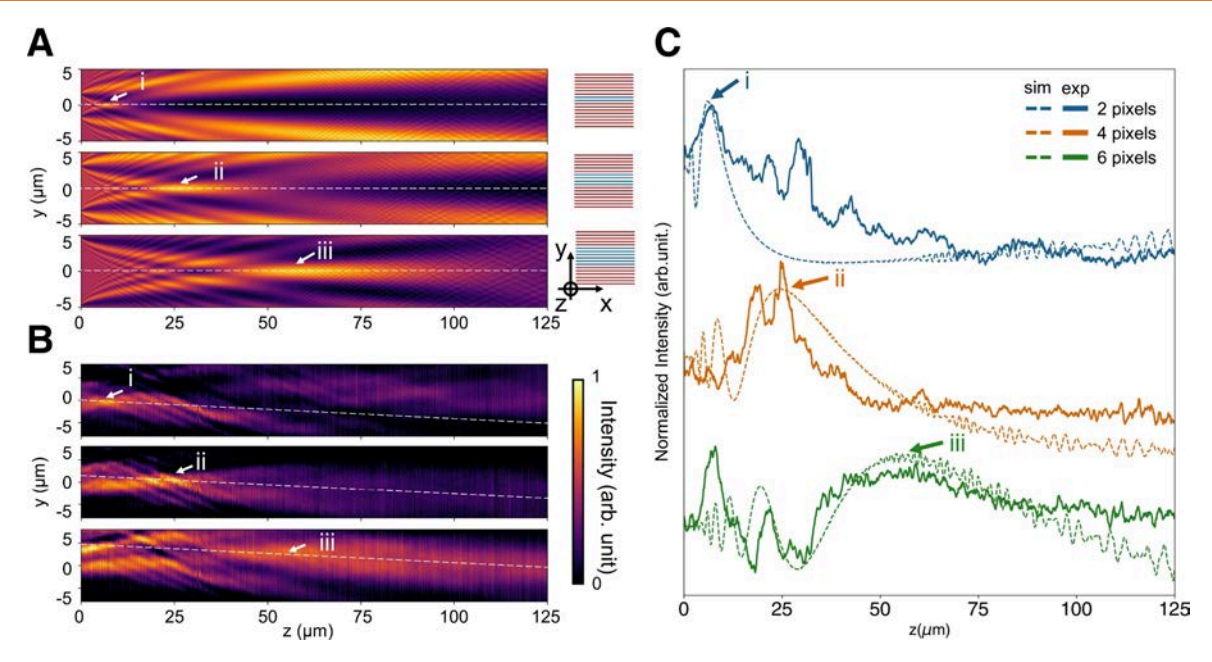


Figure 4. Demonstration of tunable far-field beam shaping. (A) Angular spectrum propagation simulation for a metasurface with 2 (top), 4 (middle), and 6 (bottom) central meta-molecules being amorphous and the rest crystalline. The schematic on the right shows the corresponding phase mask (red: crystalline, blue: amorphous). The coordinate system is indicated below the schematics, with z being the optical axis. (B) Experimentally measured beam profiles. The plotted data are normalized to the globally crystalline configuration to remove the effect of objective focusing and then averaged in the x direction over the central 10 pixels of the metasurface. The focal points in panels A and B are denoted with white arrows and labeled from i to iii. The focal points are defined as the location with the highest local intensity averaged within a 1.5  $\mu$ m  $\times$  1.5  $\mu$ m box. The near-field maxima below  $z = 50 \,\mu$ m are excluded while extracting the focal point in the last subfigure. The white dashed lines denote the optical axis, and the experimental optical axis is tilted downward because of the 3° incident angle to excite the resonance mode. (C) Simulated (dashed lines) and measured (solid lines) longitudinal intensity distributions along the optical axis. The 2-, 4-, and 6-pixel configurations are shown by "blue", "orange", and "green" lines, respectively. All three configurations show a local intensity peak at their focal planes, marked with i—iii, corresponding to in panels A and B. The experimental result agrees well with the simulation. The plotted curves are smoothened using a 21-point moving average filter. (sim: simulation, exp: experiment, arb. unit: arbitrary unit).

voltage pulses to all ON channels with an equal resistance (Supplementary Figure S8) to allow simultaneous control. Each ground channel is switched ON/OFF by a field-effect transistor switch on PCB 2, which controls the voltage drop on each metamolecule. Since our SLM is 1D, the smallest pixel size is equivalent to the 0.9  $\mu$ m diatomic period, which is necessary to excite the resonance at 1.5  $\mu$ m and significantly smaller than the  $\sim$ 10  $\mu$ m pixel size of commercial LC-SLMs. Compared to LC-SLMs, which suffer from pixel crosstalk, PCMs-based SLMs are intrinsically immune to thermal crosstalk during amorphization (due to thresholding nature of the phase transition 19,43), which makes the subwavelength pixel size possible. Limited by the number of channels (17) on current PCBs, we have to group two meta-atoms together to form a pixel, leading to an experimentally demonstrated pixel size of 1.8  $\mu$ m. The PCB can be redesigned in the future to integrate multiplexers that allow control of more channels. For example, 34 channels will lead to a pixel size of only 0.9  $\mu$ m as each pixel will consist of only one period.

We implemented arbitrary phase masks via the following two-step sequence: (1) first, all meta-molecules were electrically switched to the crystalline phase with pulse duration  $t_{\rm crys}$  (50  $\mu$ s) and channel programming energy  $E_{\rm crys}$  (1.5  $\mu$ J); (2) a single amorphization pulse with duration  $t_{\rm amor}$  (1.25  $\mu$ s) and programming energy  $E_{\rm amor}$  (0.2  $\mu$ J) was then applied to switch the selected meta-molecules. Amorphization, instead of crystallization, was used for independent control to avoid channel crosstalk. We observed large crosstalk if crystallization was used to switch the individual channel (Supplementary

Figure S9), as the longer crystallization pulses would lead to a more severe thermal dispersion (Supplementary Figure S10). Additionally, the lower temperature threshold for crystallization  $T_{\rm crys}$  compared to amorphization  $T_{\rm amor}$  ( $T_{\rm crys}$  ~200 °C vs  $T_{\rm amor}$ ~620 °C) can also contribute to crosstalk. Thanks to this crosstalk-free performance of the amorphization process, our two-step programming method can address individual pixels, albeit at the cost of additional programming time and energy. To reduce the extra time and energy consumption, we can avoid the two-step method when amorphization of channels is demanded, as it is crosstalk-free. Therefore, we will consider only the excess time and energy compared to direct crystallization below. We emphasize that, although the pause time between cycles was 2 s for thermal dissipation, such pause is not necessary for the twostep programming scheme as  $T_{\rm crys}$  is significantly lower than  $T_{\rm amor}$ . The modulation time  $t_{\rm total}$  can be estimated as  $t_{\rm cycle} = t_{\rm crys} +$  $t_{\rm amor} \approx t_{\rm crys}$ , meaning that the two-step method incurs little extra programming time for crystallization. The total programming energy  $E_{\text{total}}$  can be estimated as  $E_{\text{total}} = N_{\text{total}} \cdot E_{\text{crys}} + N_{\text{amor}} \cdot E_{\text{amor}}$ where  $N_{\text{total}} = 17$  is the total number of channels, and  $N_{\text{amor}}$  is the number of amorphous channels. The worst-case excess energy consumption  $E_{\text{excess}}$  can be estimated as  $E_{\text{excess}} = N_{\text{total}} \cdot E_{\text{crys}} +$  $(N_{\rm total} - 1) \cdot E_{\rm amor} \approx 28.7 \,\mu\text{J}$  when a single channel needs to be crystallized. To reduce the thermal crosstalk during crystallization and avoid the two-step method, one can isolate each silicon nanowire with good thermal isolators, such as using heterogeneously layered two-dimensional materials.44 Another more practical approach is to undercut the burried oxide layer such that the suspended gratings are thermally isolated by air, a

technique commonly used in silicon photonics to reduce thermal crosstalk between phase shifters.<sup>45</sup>

Using the two-step switching method, four different configurations of the metasurface were obtained, shown in the IR camera images in Figure 3C: (i) all amorphous metasurface; (ii and iii) hybrid metasurface with an amorphous period two and three times the original channel pitch, respectively, and (iv) all crystalline metasurface. Movie S1 shows the reversible switching between these configurations. The inset at the bottom left corner of each subplot shows the respective metasurface configurations. The bright (dark) lines correspond to amorphous (crystalline)  $Sb_2Se_3$  from the slight absorption difference. The patterns are implemented by the same phase transition conditions, showcasing a universal method to set arbitrary patterns. Besides the IR camera images, we also measured the spectra of the configurations in Supplementary Figure S11, which qualitatively matches with simulations.

Apart from collectively switching multiple channels, we further showed that the pixels can be independently addressed one by one (Movie S2). Increasing the number of amorphized channels caused a gradual spectral shift of the resonance from 1235 to 1228 nm, as shown in Figure 3D. We fitted the resonance to a Fano line shape and extracted the resonance shift versus the number of meta-molecules switched in Figure 3E. The small error bars averaged over nine repeated cycles suggest a highly deterministic multilevel operation. Compared to the partial amorphization of a single pixel via pulse amplitude or width modulation, individual tuning of the meta-molecules is much more reliable since each meta-molecule undergoes a full amorphization process. The resonance shift was not observed when more than 10 meta-molecules were switched because the focused probe beam with a natural Gaussian shape has low intensity at the edge. Besides the Gaussian beam shape, this observation can be also attributed to the edge effect of our relatively small metasurface (only  $\sim 30 \mu m$ ), see simulation results in Supplementary Figure S12. The fitted Q factor (Supplementary Figure S13) first decreases from ~120 to ~90 until 4 meta-molecules are switched and then increases to  $\sim$ 120. We attribute the lower Q-factor to inhomogeneous broadening, resulting from the coexistence of the amorphous and crystalline resonance mode. As more meta-molecules are switched, the amorphous resonance gradually dominates, leading to an increase of the Q-factor.

Finally, we demonstrate the device's functionality as a fully configurable spatial light modulator by independently controlling each meta-molecule to locally impart phase shifts and to manipulate the transmitted light field. This enables tunable beam focusing at different depths as different numbers of metamolecules are switched to the amorphized state. Thanks to the significant resonance shift (~10 nm), the switching induces a local phase shift near the resonance wavelength (0  $\sim 2\pi$ , dependent on the wavelength). The simulation result in Figure 4A shows a distinct change of the intensity profiles along the optical axis and achieves focusing of the transmitted light at focal lengths of 6.1, 26.4, and 60.1  $\mu$ m, as the central 2, 4, or 6 pixels are amorphized to implement a different phase pattern on the transmitted light. The focal point is defined here as the location with the maximum local intensity averaged within a 1.5  $\mu$ m  $\times$  1.5  $\mu$ m box, and the coordinate system is indicated in the inset of Figure 4A. We note that, in simulation, the phase shift was adjusted to  $1.75\pi$ , as it matched the experimental result the best.

We then measured the transmitted field intensity for the same metasurface configurations at a wavelength of 1240 nm along the

optical axis using a motorized stage <sup>46</sup> (see Methods). Figure 4B shows the measured intensity profiles, which clearly exhibit a change in the focusing behavior as the metasurface is set to the respective phase profiles. Importantly, from measurements, we obtain maximum field intensities along the optical axis at z = 6.6, 25.7, and 62.5  $\mu$ m, closely matching the simulation.

We note that, although the longitudinal intensity profiles closely match in the experiment and simulation, the width of the focal spot in the experiment appears more divergent. We primarily attribute this to the relatively broad line width of our laser source of ~1 nm (Supplementary Figure S14), which smears out the optical phase contrast over a wider phase range. However, this issue can be directly addressed by employing a tunable laser source with narrower line width, which are commercially available (~1 pm).

To emphasize the change in the field intensity and the close match between simulation and experiment, Figure 4C shows the intensity distributions along the optical axis (white dashed lines in Figure 4A,B). We note that this axis is tilted in the experimental result because of the small incident angle ( $\sim$ 3°) necessary to excite the guided-mode resonance (Supplementary Figure S7). Besides the closely matching focal spots, we also observed abnormal intensity maxima at around 10  $\mu$ m in the 6-meta-molecule configuration (green line in Figure 4C), which are attributed to strong near-field interactions.

While the tunable focusing demonstration is a proof of the functionality for the device, further improvement can be directly achieved by increasing the pixel number in future iterations. Ultimately, this will extend the far-field beam shaping scheme to more complex tasks, such as beam steering and vortex beam generation, as a larger number of controllable meta-molecules becomes available.

## **CONCLUSIONS**

In this work, we developed an electrically reconfigurable, transmissive metasurface that enables optical phase modulation in a nonvolatile fashion. Importantly, we showcased individualpixel controllability with little mutual pixel crosstalk, making it a spatial light modulator. We experimentally demonstrated a strong phase-only modulation ( $\sim 0.2\pi$ ) with less than 10% change in intensity, enabled by the coupling of a thin layer of low-loss phase-change material Sb<sub>2</sub>Se<sub>3</sub> to a high-Q q-BIC metasurface. The achievable phase modulation was 10 times larger than a blanket layer without coupling to a metasurface. The device was robust against switching for over 1000 times without degradation in performance. We further exploited a different resonance mode in the same structure to achieve a much larger resonance shift ( $\sim$ 8 nm) and  $2\pi$  phase shift with individual meta-molecule control, supporting 10 highly deterministic resonance levels. Finally, tunable far-field beam shaping with three different focal lengths was demonstrated by imparting different phase profiles, showcasing the capability of our SLM for free-space light manipulation.

Although we are limited to operation with distinct phase values at a specific wavelength, further work will explore full  $2\pi$  phase-only control by carefully designing an avoided crossing between an overcoupled resonance and resonance with high frequency tunability.<sup>38</sup> Huygen's metasurfaces with spectrally overlapped magnetic and electric dipole resonances can also be used to achieve  $2\pi$  phase shift with unity transmission.<sup>26</sup> Although currently the SLM is 1D, a 2D SLM can be realized in the future based on a cross-bar array via a two-transistor-one-

capacitor (2T1C) configuration, which is a mature technology in the display community.<sup>47</sup>

We note that our current device only supports near-resonant operation, whose bandwidth is inherently limited for almost any resonant structures. One solution for broadband operation is to harness PCMs with colossal refractive index contrast  $\Delta n$ between the amorphous and crystalline phases, such as  $Ge_2Sb_2Te_5$  ( $\Delta n \sim 3$  at 1,550 nm), which still necessitates a ~0.5  $\mu$ m thickness to reach  $2\pi$  phase shift. Moreover,  $Ge_2Sb_2Te_5$ cannot provide phase-only modulation due to its huge absorption loss in the crystalline phase. Another potential approach is to explore the idea of omni-resonance.<sup>48</sup> Omniresonance is a broadband resonance enabled by matching the incident angles of each wavelength with the energy-momentum spectrum (also known as the E-k spectrum) of the resonant structure. However, this approach will limit the system's field of view (FOV) because of the stringent angle-wavelength matching condition. Importantly, we would like to point out that even single wavelength operation can readily meet the requirement of many important applications such as LiDAR<sup>4</sup> and computergenerated holography. 49

We simulated the E-k spectrum for the quasi-BIC mode and guided-mode resonance (Supplementary Figure S15) and found that both modes are highly sensitive to the incident angle. This angle dependence is undesirable in SLMs as it limits the input FOV. One potential way to produce an angle-independent resonance is to use flatband resonant metasurfaces, <sup>50,51</sup> typically realized by partially etching a thick silicon layer and breaking the vertical symmetry of the metasurface. Such a design does not conflict with our existing diatomic grating design as we show one such flatband diatomic metasurface design in Supplementary Figure S15. One potential technical difficulty is that the bottom unetched silicon should be undoped to support individual channel control, but such vertical junction has been demonstrated in previous works <sup>52</sup> and could be achieved by carefully optimizing the annealing process for dopant activation.

Overall, our work shows nonvolatile transmissive phase SLMs with zero-static power consumption. The inherent memory of our device is crucial to simplifying the electronic circuits for individual-pixel control. The thinness of the pixels (silicon and  $\mathrm{Sb}_2\mathrm{Se}_3$ , ~240 nm) further boasts a low mutual pixel crosstalk, hence a compact pixel size and large FOV. Ultimately, we envision that, with more independently controllable pixels, this device holds promise for various applications, such as semistatic display, <sup>53</sup> structured light generation, <sup>54,55</sup> free-space optical neural networks, <sup>56</sup> and AR/VR. <sup>57</sup>

### **METHODS**

Device Fabrication. The reconfigurable diatomic metasurface is fabricated on a 220 nm thick silicon layer on top of a 3  $\mu$ m thick buried oxide layer (SOITECH) with back-side-polished silicon. The blanket SOI wafer is first implanted by phosphorus ions with a dosage of 2 ×  $10^{15}$  cm<sup>-2</sup> and an ion energy of 40 keV at a tilt angle of 7°. Subsequently, the wafer is annealed at 950  $^{\circ}$ C for 30 min to activate the dopants. The metasurface pattern is defined by a JEOLJBX-6300FS 100 kV electronbeam lithography (EBL) system using positive tone ZEP-520A resist. 220 nm fully etched gratings are made by an inductively coupled plasma reactive ion etching (ICP-RIE) process in florine-based gases. Before metallization, the surface native oxide was removed by immersing the chips in 10:1 buffered oxide etchant (BOE) for 15 s to ensure Ohmic contact. A second EBL exposure using positive tone poly(methyl methacrylate) (PMMA) resist is subsequently carried out to create windows for the Ti/Au deposition. After development, 5 nm Ti followed by 150 nm Au was electron-beam evaporated onto the chip.

The lift-off of Ti/Au was completed again by immersing the chip in methylene chloride. Note that, for the individual control of metamolecules, we replaced Au with Pt for electrodes to avoid the melting of the traces at high voltages. The third EBL step is used to expose the PMMA resist before depositing Sb<sub>2</sub>Se<sub>3</sub> via magnetron sputtering. The Sb<sub>2</sub>Se<sub>3</sub> is sputtered using a magnetron sputtering system at 30 W RF power under a deposition pressure of 4 mTorr and an Ar flow of 30 sccm. The deposition rate for  $Sb_2Se_3$  is  $\sim 1$  nm/min. Additionally, the samples are capped with 10 nm of SiO<sub>2</sub> sputtered in situ (150 W RF power, 4 mTorr pressure, and Ar flow of 30 sccm) to prevent oxidation during sample shipping. The atomic ratio of Sb<sub>2</sub>Se<sub>3</sub> after deposition is confirmed using XPS to be Sb:Se  $\approx$  44:56, which is close to the sputtering target stoichiometry of Sb:Se ≈ 40:60. Immediately after lifting off the PCM in methylene chloride, a 40 nm ALD Al<sub>2</sub>O<sub>3</sub> is grown on the chip to protect the PCM from oxidation and reflowing during switching. To allow good adhesion between the wedge bonds and metal pads, the fifth EBL step is used to open windows in the PMMA resist at the wire bonding regions for Al<sub>2</sub>O<sub>3</sub> etching. The Al<sub>2</sub>O<sub>3</sub> on top of the contacts is etched away using ICP-RIE etching in chlorine-based gases. Then, the PCMs are initialized into the fully crystalline state by rapid thermal annealing (RTA) at 200 °C for 10 min under a N<sub>2</sub> atmosphere. Finally, the chip is wire-bonded onto the custom-made PCBs using a wire bonder (Westbond) via gold ball-wedge bonds.

**Optical Spectral Measurement.** The metasurface is characterized by a custom-built two-objective transmission setup (see Figure 2B and Supplementary Figure S16a). A collimated broadband laser (Fianium) is linearly polarized and focused onto the metasurface at normal incidence by a 10× near IR objective (Mitutoyo, 0.26 numerical aperture) and collected by a 50× near IR objective (Olympus, 0.65 numerical aperture). The beam splitter (Transmission: Reflection  $\sim$ 85:15 in near IR) splits the light into two paths: one path ( $\sim$ 85%) goes to the IR spectrometer (Princeton Instrument) for characterizing the optical spectrum; the other path (~15%) goes to the IR camera (NIT SenS 320) for imaging the metasurface. Supplementary Figure 16b shows the modified setup for characterizing the cyclability of the tunable mesurface and beam splitting. A tunable continuous-wave laser (Santec TSL-510) is used here as the source to park the laser wavelength near the 1518 nm resonance, while the real-time transmission is monitored by a low-noise power meter (Keysight 81634B). To extract the *Q* factor, the diatomic resonance is fitted by a

Fano line shape using the equation  $T = \left| a + jb + \frac{c}{E - E_0 + j\gamma} \right|^2$ , where a, b, and c are constant real numbers. E is the photon energy, and  $E_0$  is the central resonance energy.  $2\gamma$  is the line width of the resonance. So, the Q factor is calculated to be  $\frac{E_0}{2\gamma}$ .

**Optical Phase Measurement.** To measure the phase shift caused by the switching, we built a Mach—Zehnder interferometer (Supplementary Figure S16b) and switched the pixel *in situ*. The interference fringes between the signal beam through the metasurface and the reference beam are taken by the IR camera. The images are captured at 11 different wavelengths from 1513 to 1523 nm for the two optical states, averaged over 20 frames. The phase of each optical state is calculated by first applying a high pass filter on the image in the Fourier domain, and then take the argument of the filtered image in the real space. The phase shift is the difference between the extracted phase in the crystalline state and amorphous state.

Electrical Control for Individual Addressing. Each metasurface pixel on the chip is connected to a metal pad that is wire-bonded to a pin on the carrier PCB or PCB1. A hole (0.8 cm in diameter) is opened at the center of PCB1 to allow direct light transmission through the PCB. To individually control the pixels, a second customized PCB (PCB2) carrying a microcontroller (Arduino Nano) is inserted into the predefined pins on PCB1. Most commercial microcontrollers normally supply low voltage ( $\leq$ 5 V) and slow speed (tens of megahertz), whereas high amplitude (>10 V) and short (nanosecond falling edge) pulses are required to amorphized the PCMs. Hence the microcontroller cannot be directly used to switch PCMs, instead an external function generator (Keysight 81150A) is connected to the PCB2 as a source of excitation. The microcontroller can be programmed to turn on/off 17 field-effect

transistors connected in series with the on-chip microheaters. By switching the field-effect transistors, the voltage drop across the microheater can be controlled independently when an electrical pulse is applied. The resistance of the microheaters is measured using a source meter (Keithley 2450). A 30  $\mu$ m  $\times$  30  $\mu$ m large metasurface pixel typically has resistance of  $\sim$ 115  $\Omega$  at 1 mV DC bias, with  $\sim$ 45  $\Omega$  due to the relatively long Pt wires. The resistance of a single channel is  $\sim 1.45$  $k\Omega$ . To reconfigure the metasurface, we used a voltage pulse of 15 V (~10 mA/channel), a 1.25  $\mu$ s pulse width, and an 8 ns rising/trailing edge to induce the amorphization. For crystallization, multiple voltage pulses of 6 V ( $\sim$ 4.1 mA/channel), 50  $\mu$ s pulse width, and 30  $\mu$ s trailing edge are used. Our current device size is limited by the maximum voltage (20 V at 50  $\Omega$  load impedance) of our function generator. A larger aperture size will require function generator that can source higher voltage to amorphize the PCMs, for example, a previous work shows electrically switching of a larger PCM-based metasurface with 150  $\mu$ m × 150  $\mu$ m area using 23 V, 5  $\mu$ s amorphization pulses.<sup>7</sup> However, we do not believe increasing the voltage is practical since a high-voltage function generator is already rare, and it is even harder to generate high voltage and withstand high current in a CMOS circuit. Instead, one can tile the 30  $\mu$ m  $\times$  30  $\mu$ m metasurface pixel in 2D to obtain a larger area while maintaining a relative low voltage requirement, although at the cost of a more complex control circuit.

Beam Focusing Simulation and Measurement. We used a 2D angular spectrum propagation program for the beam focusing simulation. A uniform input field distribution was assumed that imparts on the metasurface with center 2, 4, and 6 pixels with a  $1.75\pi$  phase and 0 everywhere else. After transmission through the metasurface, the beam is numerically propagated in the momentum space and transformed back to real space to obtain the intensity distribution at specific z positions. In the experiment (see Supplementary Figure S16c), a broadband laser source (SuperK FIANIUM) with a tunable multichannel filter (SuperK SELECT) is used to provide light near 1230 nm. To further reduce the line width, a dispersive grating was used before coupling the laser to the optical fiber, which reduced the line width from  $\sim$ 15 nm to  $\sim$ 1 nm. The laser is collimated at the other end of the fiber, filtered by an iris, focused by a 10× NIR objective (Mitutoyo, 0.26 numerical aperture) on the metasurface to provide enough intensity. An imaging system, consisting of a 50× near IR objective (Olympus, 0.65 numerical aperture), a lens (Thorlabs AC254-200-C, f = 200 mm), and an IR camera is on a z motor stage. The raw data are videos (PTW files) taken by the IR camera with an exposure time of 1 ms and a frame rate of 50 frames/s, while the motor stage moves away from the metasurface imaging plane with a velocity of 5  $\mu$ m/second. All frames are then processed in MATLAB to obtain the cross-sectional intensity profile at each z-step. The results are normalized to the global crystalline metasurface data to compensate for the slight focusing due to the 10× objective.

## **ASSOCIATED CONTENT**

## **Data Availability Statement**

All data needed to evaluate the conclusions in the paper are present in the paper and/or the Supporting Information.

# **Supporting Information**

The Supporting Information is available free of charge at https://pubs.acs.org/doi/10.1021/acsnano.4c00340.

Reversible switching between different configurations in Figure 3C (MP4)

Individually address each pixel one by one in Figure 3D,E

Figure S1 shows the simulated electrical field amplitude of the quasi-BIC resonance in diatomic grating structure, Figure S2 shows the resonance fitting to experimental results for the quasi-BIC mode for both amorphous and crystalline Sb<sub>2</sub>Se<sub>3</sub>, Figure S3 shows a broad (no) optical resonance after capping 20 nm a(c)-GST on the diatomic grating metasurface due to high absorption loss of GST,

Figure S4 shows the temporal response of the reversible switching, indicating a nonvolatile response, Figure S5 shows the optical micrographs of the metasurface pixel before and after the cyclability test, indicating a uniform switching and little damage after over 1000 cycles, Figure S6 shows the reversible switching of the GST blanket film, Figure S7 shows the optimized metal wire geometry to achieve equal resistance across 17 channels, Figure S8 shows the simulated and measured optical response of the TE-polarized guided-mode resonance with strong field overlap with Sb<sub>2</sub>Se<sub>3</sub>, achieving larger resonance shift and a full  $2\pi$  phase modulation with only small amplitude change, Figure S9 shows the evidence of thermal crosstalk-free performance during the amorphization process from repeated switching experiments, Figure S10 shows the Joule heating simulation in COMSOL for understanding of the thermal crosstalk-free performance during amorphization, Figure S11 shows the measured transmission spectra for four different programmed configurations in Figure 3c, further indicating the excellent programmability, Figure S12 shows the simulated evidence of the edge effect, where a weaker resonance shift is observed when switching meta-atoms at the edge, Figure S13 shows the fitted Q-factor of the metasurface versus the number of switched metamolecules, Figure S14 shows the spectrum of the Fianium broadband source combined with a grating, Figure S15 shows the simulated energy-momentum spectrum for both resonance modes and a different diatomic grating metasurface design with flatband performance for wide input FOV, Figure S16 shows the optical measurement setup with in situ electrical control of metasurface, and Supplementary Table S1 compares our Sb<sub>2</sub>Se<sub>3</sub>-based nonvolatile transmissive SLMs with other SLMs, including both commercial and lab-made LC-SLMs. (PDF)

# **AUTHOR INFORMATION**

# **Corresponding Authors**

**Zhuoran Fang** – Department of Electrical and Computer Engineering, University of Washington, Seattle, Washington 98195, United States; o orcid.org/0000-0001-8724-6633; Email: rogefzr@uw.edu

Rui Chen – Department of Electrical and Computer Engineering, University of Washington, Seattle, Washington 98195, United States; o orcid.org/0000-0001-8492-729X; Email: charey@uw.edu

Arka Majumdar - Department of Electrical and Computer Engineering and Department of Physics, University of Washington, Seattle, Washington 98195, United States; orcid.org/0000-0003-0917-590X; Email: arka@uw.edu

## **Authors**

ı

Johannes E. Fröch - Department of Electrical and Computer Engineering and Department of Physics, University of Washington, Seattle, Washington 98195, United States

Quentin A. A. Tanguy – Department of Electrical and Computer Engineering, University of Washington, Seattle, Washington 98195, United States

Asir Intisar Khan – Department of Electrical Engineering, Stanford University, Stanford, California 94305, United States; orcid.org/0000-0003-4635-4667

- Xiangjin Wu Department of Electrical Engineering, Stanford University, Stanford, California 94305, United States
- Virat Tara Department of Electrical and Computer Engineering, University of Washington, Seattle, Washington 98195, United States
- Arnab Manna Department of Physics, University of Washington, Seattle, Washington 98195, United States; orcid.org/0009-0007-0056-9650
- David Sharp Department of Physics, University of Washington, Seattle, Washington 98195, United States; orcid.org/0000-0002-1034-8567
- Christopher Munley Department of Physics, University of Washington, Seattle, Washington 98195, United States; orcid.org/0000-0001-5684-3144
- Forrest Miller Department of Electrical and Computer Engineering, University of Washington, Seattle, Washington 98195, United States; The Charles Stark Draper Laboratory, Cambridge, Massachusetts 02139, United States; orcid.org/0009-0000-1840-4204
- Yang Zhao Department of Electrical and Computer Engineering, University of Washington, Seattle, Washington 98195, United States
- Sarah Geiger The Charles Stark Draper Laboratory, Cambridge, Massachusetts 02139, United States
- Karl F. Böhringer Department of Electrical and Computer Engineering and Institute for Nano-engineered Systems, University of Washington, Seattle, Washington 98195, United States; Orcid.org/0000-0002-9428-2648
- Matthew S. Reynolds Department of Electrical and Computer Engineering, University of Washington, Seattle, Washington 98195, United States
- Eric Pop Department of Electrical Engineering, Stanford University, Stanford, California 94305, United States; orcid.org/0000-0003-0436-8534

Complete contact information is available at: https://pubs.acs.org/10.1021/acsnano.4c00340

### **Author Contributions**

<sup>#</sup>Z.F. and R.C. contributed equally to this work. Z.F. and A.M. conceived the project. Z.F. designed and fabricated the tunable diatomic metasurfaces, designed the printed circuit boards (PCBs), performed the spectral, phase, and cyclability measurements. R.C. designed and fabricated the independently tunable meta-molecules and performed the independent switching, multilevel operation, and dynamic beam focusing measurements. Z.F. and R.C. analyzed the data. J.E.F. built the optical setup for conducting spectral, phase, and focusing measurements. Q.A.A.T. and K.F.B. helped with the design of PCBs and wire bonding. A.I.K. and X.W. performed the Sb<sub>2</sub>Se<sub>3</sub> deposition. V.T., A.M., D.S., C.M., Y.Z., F.M., and S.G. helped with the design and measurements. M.S.R. helped with the PCB design. E.P. facilitated the Sb<sub>2</sub>Se<sub>3</sub> deposition. A.M. supervised the project. Z.F. and R.C. wrote the manuscript with input from all authors. All authors have given approval to the final version of the manuscript.

# Notes

The authors declare no competing financial interest. This work has a preprint version prior to publication in ACS Nano: Fang, Z.; Chen, R.; Fröch, J. E.; Tanguy, Q. A.; Khan, A. I.; Wu, X.; Tara, V.; Manna, A.; Sharp, D.; Munley, C; Miller, F; Zhao, Y.; Geiger, S. J.; Böhringer, K. F.; Reynolds, M.; Pop, E.; Majumdar A. Nonvolatile Phase-only Transmissive Spatial Light

Modulators. 2023, arXiv:2307.12103. arXiv preprint. https://arxiv.org/abs/2307.12103. (accessed Mar 09, 2024).

# **ACKNOWLEDGMENTS**

The research is funded by National Science Foundation (NSF-1640986, NSF-2003509), ONR-YIP Award, DRAPER Laboratories, DARPA-YFA Award, and Intel. F.M. is supported by a Draper Scholars Program. Part of this work was conducted at the Washington Nanofabrication Facility/Molecular Analysis Facility, a National Nanotechnology Coordinated Infrastructure (NNCI) site at the University of Washington with partial support from the National Science Foundation via awards NNCI-1542101 and NNCI-2025489.

#### REFERENCES

- (1) Johnson, K. M.; McKnight, D. J.; Underwood, I. Smart Spatial Light Modulators Using Liquid Crystals on Silicon. *IEEE J. Quantum Electron.* **1993**, 29, 699–714.
- (2) Hornbeck, L. J. Deformable-Mirror Spatial Light Modulators. In *Spatial Light Modulators and Applications III*; SPIE, 1990; Vol. 1150, pp 86–103.
- (3) Li, S.-Q.; Xu, X.; Maruthiyodan Veetil, R.; Valuckas, V.; Paniagua-Domínguez, R.; Kuznetsov, A. I. Phase-Only Transmissive Spatial Light Modulator Based on Tunable Dielectric Metasurface. *Science* **2019**, 364, 1087–1090.
- (4) Park, J.; Jeong, B. G.; Kim, S. I.; Lee, D.; Kim, J.; Shin, C.; Lee, C. B.; Otsuka, T.; Kyoung, J.; Kim, S.; Yang, K.-Y.; Park, Y.-Y.; Lee, J.; Hwang, I.; Jang, J.; Song, S. H.; Brongersma, M. L.; Ha, K.; Hwang, S.-W.; Choo, H.; Choi, B. L. All-Solid-State Spatial Light Modulator with Independent Phase and Amplitude Control for Three-Dimensional LiDAR Applications. *Nat. Nanotechnol.* **2021**, *16*, 69–76.
- (5) Benea-Chelmus, I.-C.; Meretska, M. L.; Elder, D. L.; Tamagnone, M.; Dalton, L. R.; Capasso, F. Electro-Optic Spatial Light Modulator from an Engineered Organic Layer. *Nat. Commun.* **2021**, *12*, 5928.
- (6) Wang, Y.; Landreman, P.; Schoen, D.; Okabe, K.; Marshall, A.; Celano, U.; Wong, H.-S. P.; Park, J.; Brongersma, M. L. Electrical Tuning of Phase-Change Antennas and Metasurfaces. *Nat. Nanotechnol.* **2021**, *16*, 667–672.
- (7) Zhang, Y.; Fowler, C.; Liang, J.; Azhar, B.; Shalaginov, M. Y.; Deckoff-Jones, S.; An, S.; Chou, J. B.; Roberts, C. M.; Liberman, V.; Kang, M.; Ríos, C.; Richardson, K. A.; Rivero-Baleine, C.; Gu, T.; Zhang, H.; Hu, J. Electrically Reconfigurable Non-Volatile Metasurface Using Low-Loss Optical Phase-Change Material. *Nat. Nanotechnol.* **2021**, *16*, 661–666.
- (8) Wang, Q.; Rogers, E. T. F.; Gholipour, B.; Wang, C.-M.; Yuan, G.; Teng, J.; Zheludev, N. I. Optically Reconfigurable Metasurfaces and Photonic Devices Based on Phase Change Materials. *Nat. Photonics* **2016**, *10*, 60–65.
- (9) van de Groep, J.; Song, J.-H.; Celano, U.; Li, Q.; Kik, P. G.; Brongersma, M. L. Exciton Resonance Tuning of an Atomically Thin Lens. *Nat. Photonics* **2020**, *14*, 426–430.
- (10) Wu, P. C.; Pala, R. A.; Kafaie Shirmanesh, G.; Cheng, W.-H.; Sokhoyan, R.; Grajower, M.; Alam, M. Z.; Lee, D.; Atwater, H. A. Dynamic beam steering with all-dielectric electro-optic III—V multiple-quantum-well metasurfaces. *Nat. Commun.* **2019**, *10*, 3654.
- (11) Karst, J.; Floess, M.; Ubl, M.; Dingler, C.; Malacrida, C.; Steinle, T.; Ludwigs, S.; Hentschel, M.; Giessen, H. Electrically Switchable Metallic Polymer Nanoantennas. *Science* **2021**, *374*, 612–616.
- (12) Sherrott, M. C.; Hon, P. W. C.; Fountaine, K. T.; Garcia, J. C.; Ponti, S. M.; Brar, V. W.; Sweatlock, L. A.; Atwater, H. A. Experimental Demonstration of > 230° Phase Modulation in Gate-Tunable Graphene—Gold Reconfigurable Mid-Infrared Metasurfaces. *Nano Lett.* 2017, *17*, 3027—3034.
- (13) Benea-Chelmus, I.-C.; Mason, S.; Meretska, M. L.; Elder, D. L.; Kazakov, D.; Shams-Ansari, A.; Dalton, L. R.; Capasso, F. Gigahertz Free-Space Electro-Optic Modulators Based on Mie Resonances. *Nat. Commun.* **2022**, *13*, 3170.

- (14) Persson, M.; Engström, D.; Goksör, M. Reducing the Effect of Pixel Crosstalk in Phase Only Spatial Light Modulators. *Opt. Express* **2012**, *20*, 22334–22343.
- (15) García-Márquez, J.; López, V.; González-Vega, A.; Noé, E. Flicker Minimization in an LCoS Spatial Light Modulator. *Opt. Express* **2012**, *20*, 8431–8441.
- (16) Abdollahramezani, S.; Hemmatyar, O.; Taghinejad, H.; Krasnok, A.; Kiarashinejad, Y.; Zandehshahvar, M.; Alù, A.; Adibi, A. Tunable Nanophotonics Enabled by Chalcogenide Phase-Change Materials. *Nanophotonics* **2020**, *9*, 1189–1241.
- (17) Raoux, S.; Xiong, F.; Wuttig, M.; Pop, E. Phase Change Materials and Phase Change Memory. MRS Bull. 2014, 39, 703–710.
- (18) Shportko, K.; Kremers, S.; Woda, M.; Lencer, D.; Robertson, J.; Wuttig, M. Resonant Bonding in Crystalline Phase-Change Materials. *Nat. Mater.* **2008**, *7*, 653–658.
- (19) Fang, Z.; Chen, R.; Zheng, J.; Majumdar, A. Non-Volatile Reconfigurable Silicon Photonics Based on Phase-Change Materials. *IEEE J. Sel. Top. Quantum Electron.* **2021**, 28, 8200317 DOI: 10.1109/JSTQE.2021.3120713.
- (20) Shalaginov, M. Y.; An, S.; Zhang, Y.; Yang, F.; Su, P.; Liberman, V.; Chou, J. B.; Roberts, C. M.; Kang, M.; Rios, C.; Du, Q.; Fowler, C.; Agarwal, A.; Richardson, K. A.; Rivero-Baleine, C.; Zhang, H.; Hu, J.; Gu, T. Reconfigurable All-Dielectric Metalens with Diffraction-Limited Performance. *Nat. Commun.* **2021**, *12*, 1225.
- (21) de Galarreta, C. R.; Alexeev, A. M.; Au, Y.; Lopez-Garcia, M.; Klemm, M.; Cryan, M.; Bertolotti, J.; Wright, C. D. Nonvolatile Reconfigurable Phase-Change Metadevices for Beam Steering in the Near Infrared. *Adv. Funct. Mater.* **2018**, 28, 1704993.
- (22) Chu, C. H.; Tseng, M. L.; Chen, J.; Wu, P. C.; Chen, Y.-H.; Wang, H.-C.; Chen, T.-Y.; Hsieh, W. T.; Wu, H. J.; Sun, G.; Tsai, D. P. Active Dielectric Metasurface Based on Phase-Change Medium. *Laser Photonics Rev.* **2016**, *10*, 986–994.
- (23) de Galarreta, C. R.; Sinev, I.; Alexeev, A. M.; Trofimov, P.; Ladutenko, K.; Garcia-Cuevas Carrillo, S.; Gemo, E.; Baldycheva, A.; Bertolotti, J.; Wright, C. D. Reconfigurable Multilevel Control of Hybrid All-Dielectric Phase-Change Metasurfaces. *Optica* **2020**, *7*, 476–484.
- (24) Abdollahramezani, S.; Hemmatyar, O.; Taghinejad, M.; Taghinejad, H.; Krasnok, A.; Eftekhar, A. A.; Teichrib, C.; Deshmukh, S.; El-Sayed, M. A.; Pop, E.; Wuttig, M.; Alù, A.; Cai, W.; Adibi, A. Electrically Driven Reprogrammable Phase-Change Metasurface Reaching 80% Efficiency. *Nat. Commun.* **2022**, *13*, 1696.
- (25) Julian, M. N.; Williams, C.; Borg, S.; Bartram, S.; Kim, H. J. Reversible Optical Tuning of GeSbTe Phase-Change Metasurface Spectral Filters for Mid-Wave Infrared Imaging. *Optica* **2020**, *7*, 746–754.
- (26) Leitis, A.; Heßler, A.; Wahl, S.; Wuttig, M.; Taubner, T.; Tittl, A.; Altug, H. All-Dielectric Programmable Huygens' Metasurfaces. *Adv. Funct. Mater.* **2020**, *30*, 1910259.
- (27) Moitra, P.; Wang, Y.; Liang, X.; Lu, L.; Poh, A.; Mass, T. W. W.; Simpson, R. E.; Kuznetsov, A. I.; Paniagua-Dominguez, R. Programmable Wavefront Control in the Visible Spectrum Using Low-Loss Chalcogenide Phase-Change Metasurfaces. *Adv. Mater.* **2023**, *35*, 2205367.
- (28) Delaney, M.; Zeimpekis, I.; Lawson, D.; Hewak, D. W.; Muskens, O. L. A New Family of Ultralow Loss Reversible Phase-Change Materials for Photonic Integrated Circuits: Sb<sub>2</sub>S<sub>3</sub> and Sb<sub>2</sub>Se<sub>3</sub>. *Adv. Funct. Mater.* **2020**, *30*, 2002447.
- (29) Fang, Z.; Chen, R.; Zheng, J.; Khan, A. I.; Neilson, K. M.; Geiger, S. J.; Callahan, D. M.; Moebius, M. G.; Saxena, A.; Chen, M. E.; Rios, C.; Hu, J.; Pop, E.; Majumdar, A. Ultra-Low-Energy Programmable Non-Volatile Silicon Photonics Based on Phase-Change Materials with Graphene Heaters. *Nat. Nanotechnol.* **2022**, *17*, 842–848.
- (30) Zheng, J.; Zhu, S.; Xu, P.; Dunham, S.; Majumdar, A. Modeling Electrical Switching of Nonvolatile Phase-Change Integrated Nanophotonic Structures with Graphene Heaters. *ACS Appl. Mater. Interfaces* **2020**, *12*, 21827–21836.
- (31) Wuttig, M.; Yamada, N. Phase-Change Materials for Rewriteable Data Storage. *Nat. Mater.* **2007**, *6*, 824–832.

- (32) Fang, Z.; Zheng, J.; Saxena, A.; Whitehead, J.; Chen, Y.; Majumdar, A. Non-Volatile Reconfigurable Integrated Photonics Enabled by Broadband Low-Loss Phase Change Material. *Adv. Opt. Mater.* **2021**, *9*, 2002049.
- (33) Chang-Hasnain, C. J.; Yang, W. High-Contrast Gratings for Integrated Optoelectronics. *Adv. Opt. Photonics* **2012**, *4*, 379–440.
- (34) Koshelev, K.; Lepeshov, S.; Liu, M.; Bogdanov, A.; Kivshar, Y. Asymmetric Metasurfaces with High-Q Resonances Governed by Bound States in the Continuum. *Phys. Rev. Lett.* **2018**, *121*, No. 193903.
- (35) Liu, Z.; Xu, Y.; Lin, Y.; Xiang, J.; Feng, T.; Cao, Q.; Li, J.; Lan, S.; Liu, J. High-Q Quasibound States in the Continuum for Nonlinear Metasurfaces. *Phys. Rev. Lett.* **2019**, *123*, No. 253901.
- (36) Zeng, B.; Majumdar, A.; Wang, F. Tunable Dark Modes in One-Dimensional "Diatomic" Dielectric Gratings. *Opt. Express* **2015**, *23*, 12478–12487.
- (37) Overvig, A. C.; Shrestha, S.; Yu, N. Dimerized high contrast gratings. *Nanophotonics* **2018**, *7*, 1157–1168.
- (38) Kim, J. Y.; Park, J.; Holdman, G. R.; Heiden, J. T.; Kim, S.; Brar, V. W.; Jang, M. S. Full 2 $\pi$  Tunable Phase Modulation Using Avoided Crossing of Resonances. *Nat. Commun.* **2022**, *13*, 2103.
- (39) Zheng, J.; Fang, Z.; Wu, C.; Zhu, S.; Xu, P.; Doylend, J. K.; Deshmukh, S.; Pop, E.; Dunham, S.; Li, M.; Majumdar, A. Nonvolatile Electrically Reconfigurable Integrated Photonic Switch Enabled by a Silicon PIN Diode Heater. *Adv. Mater.* **2020**, *32*, 2001218.
- (40) Ríos, C.; Du, Q.; Zhang, Y.; Popescu, C.-C.; Shalaginov, M. Y.; Miller, P.; Roberts, C.; Kang, M.; Richardson, K. A.; Gu, T.; Vitale, S. A.; Hu, J. Ultra-Compact Nonvolatile Phase Shifter Based on Electrically Reprogrammable Transparent Phase Change Materials. *PhotoniX* **2022**, *3*, 26.
- (41) Lawrence, M.; Barton, D. R.; Dixon, J.; Song, J.-H.; van de Groep, J.; Brongersma, M. L.; Dionne, J. A. High Quality Factor Phase Gradient Metasurfaces. *Nat. Nanotechnol.* **2020**, *15*, 956–961.
- (42) Zhang, H.; Zhou, L.; Lu, L.; Xu, J.; Wang, N.; Hu, H.; Rahman, B. M. A.; Zhou, Z.; Chen, J. Miniature Multilevel Optical Memristive Switch Using Phase Change Material. *ACS Photonics* **2019**, *6*, 2205–2212.
- (43) Chen, R.; Fang, Z.; Miller, F.; Rarick, H.; Fröch, J. E.; Majumdar, A. Opportunities and Challenges for Large-Scale Phase-Change Material Integrated Electro-Photonics. *ACS Photonics* **2022**, *9*, 3181–3105
- (44) Vaziri, S.; Yalon, E.; Muñoz Rojo, M.; Suryavanshi, S. V.; Zhang, H.; McClellan, C. J.; Bailey, C. S.; Smithe, K. K. H.; Gabourie, A. J.; Chen, V.; Deshmukh, S.; Bendersky, L.; Davydov, A. V.; Pop, E. Ultrahigh Thermal Isolation across Heterogeneously Layered Two-Dimensional Materials. *Sci. Adv.* 2019, 5, No. eaax1325.
- (45) Liu, S.; Feng, J.; Tian, Y.; Zhao, H.; Jin, L.; Ouyang, B.; Zhu, J.; Guo, J. Thermo-Optic Phase Shifters Based on Silicon-on-Insulator Platform: State-of-the-Art and a Review. *Front. Optoelectron.* **2022**, *15*, 9
- (46) Colburn, S.; Zhan, A.; Majumdar, A. Metasurface Optics for Full-Color Computational Imaging. *Sci. Adv.* **2018**, *4*, No. eaar2114.
- (47) Fang, Z.; Chen, R.; Tara, V.; Majumdar, A. Non-Volatile Phase-Change Materials for Programmable Photonics. *Sci. Bull.* **2023**, *68*, 783–786.
- (48) Shabahang, S.; Kondakci, H. E.; Villinger, M. L.; Perlstein, J. D.; El Halawany, A.; Abouraddy, A. F. Omni-Resonant Optical Micro-Cavity. *Sci. Rep.* **2017**, *7*, 10336.
- (49) Slinger, C.; Cameron, C.; Stanley, M. Computer-Generated Holography as a Generic Display Technology. *Computer* **2005**, 38, 46–53.
- (50) Nguyen, H. S.; Dubois, F.; Deschamps, T.; Cueff, S.; Pardon, A.; Leclercq, J.-L.; Seassal, C.; Letartre, X.; Viktorovitch, P. Symmetry Breaking in Photonic Crystals: On-Demand Dispersion from Flatband to Dirac Cones. *Phys. Rev. Lett.* **2018**, *120*, No. 066102.
- (51) Munley, C.; Manna, A.; Sharp, D.; Choi, M.; Nguyen, H. A.; Cossairt, B. M.; Li, M.; Barnard, A. W.; Majumdar, A. Visible Wavelength Flatband in a Gallium Phosphide Metasurface. *ACS Photonics* **2023**, *10*, 2456–2460.

- (52) Watts, M. R.; Zortman, W. A.; Trotter, D. C.; Young, R. W.; Lentine, A. L. Vertical Junction Silicon Microdisk Modulators and Switches. *Opt. Express* **2011**, *19*, 21989–22003.
- (53) Hosseini, P.; Wright, C. D.; Bhaskaran, H. An Optoelectronic Framework Enabled by Low-Dimensional Phase-Change Films. *Nature* **2014**, *511*, 206–211.
- (54) Wang, X.-L.; Ding, J.; Ni, W.-J.; Guo, C.-S.; Wang, H.-T. Generation of Arbitrary Vector Beams with a Spatial Light Modulator and a Common Path Interferometric Arrangement. *Opt. Lett.* **2007**, *32*, 3549–3551.
- (55) Ohtake, Y.; Ando, T.; Fukuchi, N.; Matsumoto, N.; Ito, H.; Hara, T. Universal Generation of Higher-Order Multiringed Laguerre-Gaussian Beams by Using a Spatial Light Modulator. *Opt. Lett.* **2007**, 32, 1411–1413.
- (56) Bueno, J.; Maktoobi, S.; Froehly, L.; Fischer, I.; Jacquot, M.; Larger, L.; Brunner, D. Reinforcement Learning in a Large-Scale Photonic Recurrent Neural Network. *Optica* **2018**, *5*, 756.
- (57) Gao, H.; Xu, F.; Liu, J.; Dai, Z.; Zhou, W.; Li, S.; Yu, Y.; Zheng, H. Holographic Three-Dimensional Virtual Reality and Augmented Reality Display Based on 4K-Spatial Light Modulators. *Appl. Sci.* **2019**, *9*, 1182.